ACS OMEGA

http://pubs.acs.org/journal/acsodf

Article

Comparative Study of Sonophotocatalytic, Photocatalytic, and Catalytic Activities of Magnesium and Chitosan-Doped Tin Oxide Quantum Dots

Sawaira Moeen, Muhammad Ikram,* Ali Haider, Junaid Haider, Anwar Ul-Hamid, Walid Nabgan,* Tahira Shujah, Misbah Naz, and Iram Shahzadi

Cite This: *ACS Omega* 2022, 7, 46428−46439

Read Online

ACCESS | Metrics & More | Article Recommendations

ABSTRACT: The present study demonstrates the hydrothermal synthesis of SnO_2 quantum dots (QDs) doped with different concentrations (2, 4 wt %) of magnesium (Mg) and a fixed amount of chitosan (CS). The obtained samples were investigated through a number of characterizations for optical analysis, elemental composition, crystal structure, functional group presence, interlayer spacing, and surface morphology. The XRD spectrum revealed the tetragonal structure of SnO_2 with no significant variations occurring upon the addition of CS and Mg. The crystallite size of QDs was reduced by incorporation of dopants. The optical absorption spectra revealed a red shift, assigned to the reduction of the band gap energy upon doping. TEM analysis proved that the few nanorod-like structures of CS overlapped with SnO_2 QDs, and agglomeration was observed upon Mg doping. The incorporation of dopants little enhanced the *d*-spacing of SnO_2 QDs. Moreover, the synthesized nanocatalyst was utilized to calculate the degradation percentage of methylene blue (MB) dye. Afterward, a comparative analysis of catalytic activity, photocatalytic activity, and sonophotocatalytic activity was carried out. Notably, 4% Mg/CS-doped QDs showed maximum sonophotocatalytic degradation of MB in basic medium compared to other activities. Lastly, the prepared nanocatalyst was found to be efficient for dye degradation in any environment and inexpensive.

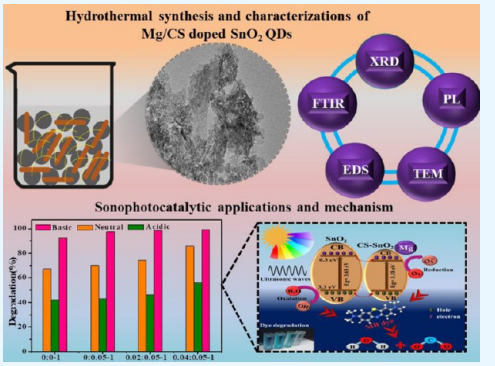

1. INTRODUCTION

At an international level, environmental pollution is creating difficulties, including insufficient availability of distilled water for a large number of people. An estimated 750 million people are facing the deficiency of unharmed and unsoiled drinking water because of the continuously increasing global population. About 97.5% of global water is saline and 2.5% is conserved for humankind's nourishment.[1] Organic dyes used in different industries such as cosmetic, paper, textile, and chemical manufacturing are sources of contaminated unsoiled water, causing a threat to the environment. Specifically, cationic dye, MB, possesses a stable aromatic structure that is non-biodegradable, posing a significant threat to aquatic life.[2] Many traditional treatments, including ion interchange, carbon filter, biological, and reverse osmosis, are used to lessen these global problems. These approaches have several restrictions, are costly and disadvantageous involving complex methods, and utilize a huge amount of energy.[3−5] Thus, logical technologies with the above-mentioned assets need to be developed; sonophotocatalytic activity (SPCA), photocatalytic activity (PCA), and catalytic activity (CA) are environmentally friendly, easy to handle, and cost-effective.[6] PCA is considered a highly optimistic approach to reduce the MB dye due to its large efficacy and ambient working conditions. However, this method is not suitable at a large scale because of the slow degradation response time and several photocatalyst disadvantages including large band gap energy (Eg) and increased electron−hole (e^--h^+) recombination.[6] To overcome these features, more modern technologies and better catalysts are required. Ultrasonic irradiation has also been extensively researched as a primary or secondary technique for the reduction of the dye. Cavitation bubbles are produced in the liquid due to ultrasonic waves. The quick collapse of the bubbles creates localized severe conditions including large pressure and large temperature, and the critical conditions cause dioxygen and water molecules to cleave, producing OH, O_2^-, and other radical species. These species have the ability to oxidize the organic contaminants in water. However, various

Received: August 10, 2022
Accepted: November 25, 2022
Published: December 9, 2022

disadvantages of the ultrasonic irradiation technique, including time-consuming reactions and utilization of a large amount of energy, have limited its applicability in dye reduction, and it has been observed that ultrasonic irradiation alone is not very efficient for degradation of pollutants. To resolve this issue, several efforts have been devoted to combine the ultrasonic irradiation process with an advanced oxidation process (AOP) like PCA. The degradation of dyes is increased in ultrasonication coupled with photocatalysis (sonophotocatalysis) due to the production of a large number of active species radicals.[7−10]

During the last few decades, in the area of environmental growth, semiconductor nanomaterials have initiated an excellent curiosity in researchers on account of the exceptional physicochemical characteristics, including nontoxicity and environmental sustainability.[11] Various approaches to synthesize metal oxides such as TiO_2 (sol−gel technique, nanoparticles with a spherical morphology),[12] CeO_2 (coprecipitation technique, QDs),[13] ZnO (chemical precipitation method, nanorods),[14] SnO_2 (hydrothermal method, spherical-shaped nanoparticles),[15] etc. are used for reduction of the MB dye.[16] Among these, hydrothermally synthesized SnO_2 QDs have attracted a significant deal of research interest in view of the exceptional optical and electrical characteristics such as low resistive power, large specific capacity, and appropriate Eg (3.6 eV). Moreover, SnO_2 QDs have large electron flexibility (∼100 to 200 $cm^2\ V^{-1}s^{-1}$), revealing a rapid transfer of photoexcited electrons.[15,17] As a result, SnO_2 is considered to be an excellent photocatalyst. Pure SnO_2 is rarely used in PCA, perhaps because of the difficulty of simultaneous synthesis of Sn^{2+} and even Sn^0, which implies that mixed phases of SnO_2 and SnO or Sn are present in the catalyst.[7] However, SnO_2 has a limitation in degrading dyes due to the large Eg and the inability to utilize visible sunlight.[18] Several efforts have been undertaken to overcome these problems by enhancing the photocatalytic degradation rate of SnO_2 by doping polymer composites such as chitosan (CS), cellulose, and starch. Among these, CS is found to be a plenteous natural biopolymer extensively used in water remediation possessing exceptional properties, including inexpensiveness, nontoxicity, and bio- and eco-friendliness [15]. Hydroxyl (−OH) and amino groups ($-NH_2$) in CS impart various antimicrobial activities, gas sensing, and wastewater treatment capability. SnO_2 QDs can utilize visible light for dye degradation by doping CS, as the Eg is reduced.[19,20] The SPCA and PCA of SnO_2 QDs can be further increased by metal doping, which modifies the SnO_2 photocatalyst to operate efficiently in visible light. The behavior of dopant ions, their quantity, the technique used for doping, and the mechanism of lowering Eg depend upon the PCA of SnO_2 by metal doping.[21−23] By doping alkaline metals including Ca, Mg, Ca, and Ra, the Eg is reduced, enhancing the dye degradation activity of SnO_2. The alkaline metal-doped SnO_2 generates lattice defects such as oxygen vacancies and facilitates the production of reactive oxygen species (ROS) that improve the PCA of SnO_2 QDs. Hence, we choose alkaline earth metals as dopants.[24]

This work presents the novel synthesis of Mg/CS-doped SnO_2 QDs by utilizing a hydrothermal technique to compare SPCA, PCA, and CA for the degradation of the MB dye.

2. EXPERIMENTAL PART

2.1. Materials. $SnCl_2{\cdot}2H_2O$, magnesium chloride hexahydrate ($H_{12}Cl_2MgO_6$ > 99%), NaOH > 98%, and chitosan ($(C_{56}H_{103}N_9O_{39}$ > 99%) were obtained from Sigma-Aldrich (Germany).

2.2. Synthesis of Mg/CS-doped SnO_2. To synthesize SnO_2 QDS by a hydrothermal method, $SnCl_2{\cdot}2H_2O$ (0.5 M) was prepared under vigorous stirring at 90 °C for 30 min. Then, an appropriate amount of NaOH solution was added to sustain pH ∼ 9 of the above-mentioned solution under stirring for 1 h. Subsequently, several concentrations of Mg were added with a fixed amount of (0.05%) CS to SnO_2 QDs in an airtight 100 mL Teflon-lined autoclave at 150 °C for 12 h. Then, the autoclaved samples were cooled at room temperature and centrifuged at 7500 rpm for 6 min. The collected sample was dried at 150 °C for 12 h and ground with a mortar and pestle to attain fine powder, as depicted in Figure 1.

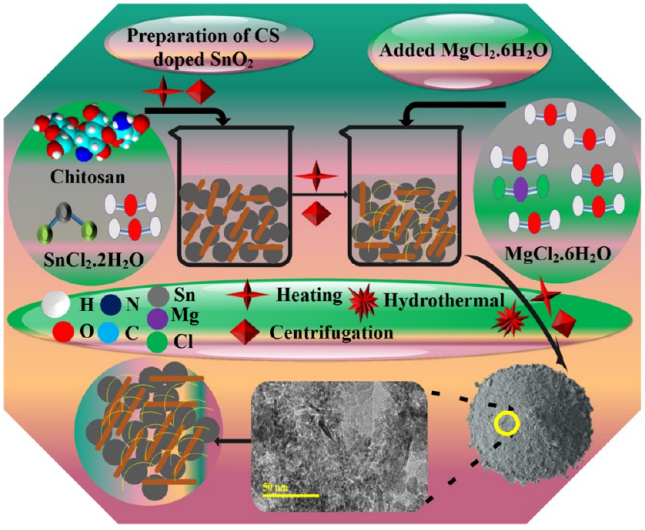

Figure 1. Schematic representation for the synthesis of Mg/CS-doped SnO_2.

2.3. Sonophotocatalytic and Photocatalytic Activity. The PCA of the pristine and doped SnO_2 was characterized in a photoreactor, and SPCA was characterized in a photoreactor containing an ultrasonic bath. The mercury lamp utilized as as visible light source in the photoreactor was 400 W with a wavelength and frequency of 400−700 nm and 430−790 THz, respectively.[25] The stock solution of MB (1 g/1 mL) with the suspension of 10 mg of photocatalyst under vigorous stirring was prepared and placed in the dark for 30 min to enable substantial absorbance. After vigorous stirring, 30 mL of each sample solution was reassigned to an ultrasonic bath in a photoreactor. The 3 mL suspension was used to determine dye reduction capability using an UV−Vis spectrophotometer. At 665 nm, the maximum absorption of MB was achieved for all samples. The efficiency of photocatalysts was calculated using the following equation

$$\%\ \text{degrdation} = (C_0 - C_t)/C_t \times 100 \quad (1)$$

where C_0 is the preliminary concentration of dye in the absence of light and C_t is the degradation concentration at constant intervals in the presence of light.

2.3.1. Reaction Mechanism and Kinetics. The reaction mechanism of PCA or SPCA for dye degradation is demonstrated in Figure 2. The SPCA and PCA start with photoexcitation, which is promoted by the photon possessing energy equal or greater than Eg. These high-energy photons

https://doi.org/10.1021/acsomega.2c05133
ACS Omega 2022, 7, 46428−46439

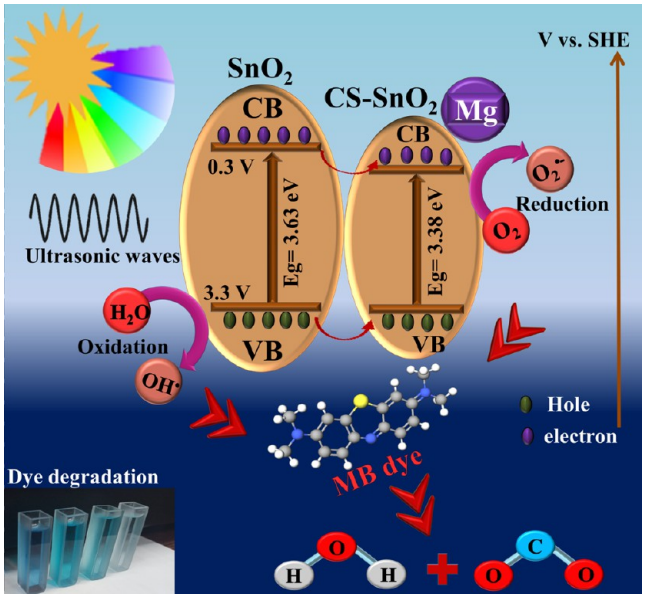

Figure 2. Sonophotoctalysis and photocatalysis mechanism of Mg/CS-doped SnO_2 QDs.

shift the valence band (VB) electron to the conduction band (CB). e^-−h^+ pairs are generated in the VB as a result of the excitation process described in the equation below

$$SnO_2 + h\nu \rightarrow e^-(CB) + h^+(VB) \quad (2)$$

The photogenerated electron reacts with O_2 to produce the superoxide radical $O_2^{\bullet-}$.

$$e^- + O_2 \rightarrow O_2^{\bullet-} \quad (3)$$

Hydroperoxyl ($HO_2^{\bullet}$) and hydroxyl radicals ($OH^{\bullet}$) are generated after the reaction of $O_2^{\bullet-}$ with water (eq 4), which play a key role in the degradation of the dye.

$$O_2^{\bullet-} + H_2O \rightarrow HO_2^{\bullet} + OH^{\bullet} \quad (4)$$

Photogenerated h^+ reacts with water to produce hydroxyl radicals ($OH^{\bullet}$).

$$h_{VB}^+ + OH^- \rightarrow OH_{ad}^{\bullet} \quad (5)$$

$$h_{VB}^+ + H_2O \rightarrow OH^{\bullet} + H^+ \quad (6)$$

Under ultrasound, acoustic cavitation pyrolyzes the H_2O molecules into $H^{\bullet}$ and $OH^{\bullet}$ and H_2O_2 is formed by combination of $OH^{\bullet}$. Finally, H_2O_2 decomposes into $OH^{\bullet}$ radicals as given below.[26]

$$SnO_2 + US))) + H_2O \rightarrow H^{\bullet} + OH^{\bullet} \quad (7)$$

$$OH^{\bullet} + OH^{\bullet} \rightarrow H_2O_2 \quad (8)$$

$$SnO_2 + US))) + H_2O_2 \rightarrow 2OH^{\bullet} \quad (9)$$

Ultimately, $OH^{\bullet}$ radicals produced by both the processes oxidize the organic molecules into CO_2 and H_2O.

$$^{\bullet}OH + \text{organic molecules} + O_2 \rightarrow \text{products}(CO_2 \text{ and } H_2O) \quad (10)$$

Moreover, even small recombination of e^-−h^+ pairs, which may be destroyed finally, will disturb the PCA of materials.

$$e_{CB}^- + h_{VB}^+ \rightarrow SnO_2 \quad (11)$$

2.4. Catalytic Activity. CA of the dopant-free and Mg/CS-doped SnO_2 QDs was analyzed in the existence of $NaBH_4$ to decolorize the dye. Initially, the desired amount of $NaBH_4$ solution was incorporated in a 3 mL MB solution, followed by introducing 400 μL of pure and (2 and 4%) Mg/CS-doped SnO_2. The dye degradation was conducted by conversion of MB to leucomethylene blue (LMB) in the presence of a reducing agent ($NaBH_4$). The reduction of MB was noticed at constant intervals with the help of an UV−Vis spectrophotometer.

2.4.1. Catalysis Mechanism. The incorporation of the synthesized catalysts and $NaBH_4$ into MB plays a key role in the catalysis mechanism, as shown in Figure 3. MB acts like an

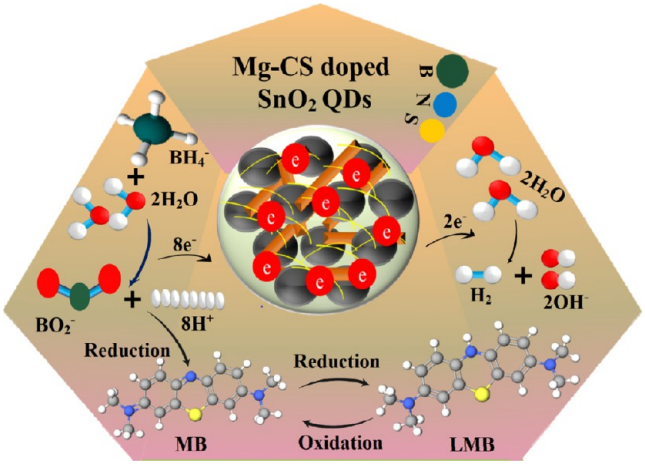

Figure 3. Schematic diagram of the catalysis mechanism of Mg/CS-doped SnO_2 QDs.

oxidizing agent, while NaBH4 works as a reducing agent. First, $NaBH_4$ split into ions and shifting an electron from the reducer to MB stimulated the redox reaction. As a result, dye degradation occurs that manifested in electron absorption in MB. Additionally, the reduction of MB in the presence of the reducing agent is slow and time-consuming.[27] The additions of the synthesized catalysts into the redox reaction act as an electron relay that permits electron shifting from a donor (BH_4^-) to MB and reduces the MB to LMB. Adsorption of MB and BH_4^- was enhanced by adding the prepared dopant-free and Mg/CS-doped SnO_2. The size of the nanocatalyst also affects the CA, as small particles possess a large surface-to-volume ratio, resulting in efficient dye reduction.[27] The two main reactions to MB degradation are shown in eqs 12 and 13.

$$BH_4^- + 2H_2O \rightarrow BO_2^- + 4H_2O \quad (12)$$

$$BH_4^- + 4MB^+ + 2H_2O \rightarrow BO_2^- + 4LMB + 4H^+ \quad (13)$$

2.5. Radical Scavenging Assay (DPPH). The free radical scavenging activity of the fabricated nanostructures was analyzed using a modified version of DPPH assay. Mg/CS-doped SnO_2 nanoparticles (50−500 μg/mL) were mixed with an equal volume of (0.1 mM) DPPH solution. This mixture was vortexed and incubated for 30 min at room temperature in the dark. A standard solution of ascorbic acid was employed as a reference sample. The degradation of the DPPH solution (λ = 517 nm) was employed to calculate the scavenging rate (%) of each sample by eq 14

https://doi.org/10.1021/acsomega.2c05133
ACS Omega 2022, 7, 46428−46439

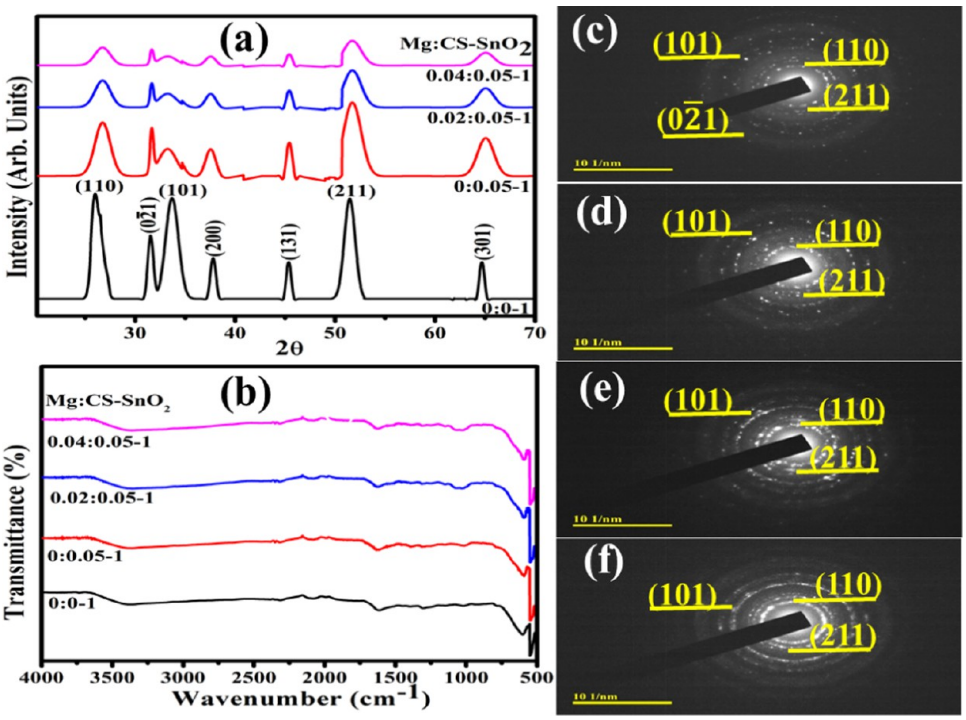

Figure 4. (a) XRD pattern, (b) FTIR spectra, and (c–f) SAED pattern of pristine and Mg/CS-doped SnO_2.

Table 1. Band Gap Energy, Average Crystallite Size, Average Particle Size, SPCA, PCA, and CA of Pure and Mg/CS-Doped SnO_2

Mg:CS-SnO_2	band gap energy (eV)	average crystallite size (nm)	average particle size (nm)	sonophotocatalytic activity in basic medium (%)	photocatalytic activity in basic medium (%)	catalytic activity in acidic medium (%)
0:0-1	3.63	9.02	9.05	92.29	87.23	61.81
0:0.05-1	3.56	8.71	9.01	97.42	91.91	66.71
0.02:0.05-1	3.47	6.32	8.56	98.37	92.72	70.18
0.04:0.05-1	3.38	5.56	6.76	99.006	96.92	73.64

$$\text{scavenging rate}(\%) = A_0 - A_1/A_0 \times 100 \quad (14)$$

Here, A_0 and A_1 = control absorbance and standard absorbance, respectively.

2.6. Characterizations. The crystal structures of SnO_2 and Mg/CS-doped QDs were investigated through a PANalytical Xpert PRO X-ray diffraction (XRD) instrument in the 2θ range of 20–70° utilizing Cu Kα radiation ($\lambda \sim 0.154$ nm). A FTIR PerkinElmer 3100 spectrometer was employed in the range of 4000–500 c/m with 32 scans to detect the existence of functional groups in the synthesized photocatalyst. To analyze the optical characteristics, a UV–Vis Genesys 10S spectrophotometer with the range of 210–600 nm was utilized. The morphological characteristics of QDs were determined using the JSM-6460LV FE-SEM scheme combined with an EDX spectrometer. PL spectroscopy of QDs was carried out using a JASCO FP-8300 system. XPS Peak 41 and Origin 9 software tools were used for binding energy calibration and peak fittings.

3. RESULTS AND DISCUSSION

XRD spectra of SnO_2 and Mg/CS-doped SnO_2 in the 2θ range from 20 to 70° are depicted in Figure 4a. Diffraction peaks were located at ~26, 33.71, 37.06, 51.34, and 65°, assigned to the (110), (101), (200), (211), and (301) facets respectively. These planes correlate to the tetragonal configuration of SnO_2 linked with the standard spectrum (JCPDS card no. 411445) along the $P42/mm$ space group. Other reflection peaks were detected at ~31.55 and 45.40° attributed to the $(0\bar{2}1)$ and (131) planes, respectively, and well-indexed with the anorthic structure of Sn_2O_3 (JCPDS no. 0251259). Upon CS doping, neither a distinct peak of the dopant nor any variations in the tetragonal configuration of SnO_2 were observed. The broadening of peaks and a significant decrease in intensity have been observed upon the introduction of CS, attributed to the intermolecular interaction and synergistic effect between CS and SnO_2 QDs.[28] Figure 4a clearly demonstrates that with Mg doping, there is no change in the phase structure; only slight shift alternation in the diffraction peak of SnO_2 can be seen. It is noted that the intensity of the diffraction peaks reduced with the increasing concentration of Mg assigned to the inclusion of Mg^{2+} into the Sn^{4+} ions, as there is a clear difference between the ionic radii of Mg^{2+} (0.072 nm) and Sn^{4+} (0.071 nm).[29] The average crystallite size of SnO_2 was calculated by the Debye–Scherrer formula, which was decreased by the incorporation of CS and Mg, as depicted in Table 1. Broad peaks upon doping of CS and Mg were observed, attributed to the decrease in the crystallite size.[30] This indicated that the existence of Mg inhibits the development of SnO_2. Other studies have found similar outcomes with different dopants in the past.[22,23] As the crystallite size reduced, the surface area of the photocatalyst becomes large, improving the adsorption of the reactant and absorption of light over the photocatalyst. Consequently, PCA

https://doi.org/10.1021/acsomega.2c05133
ACS Omega 2022, 7, 46428–46439

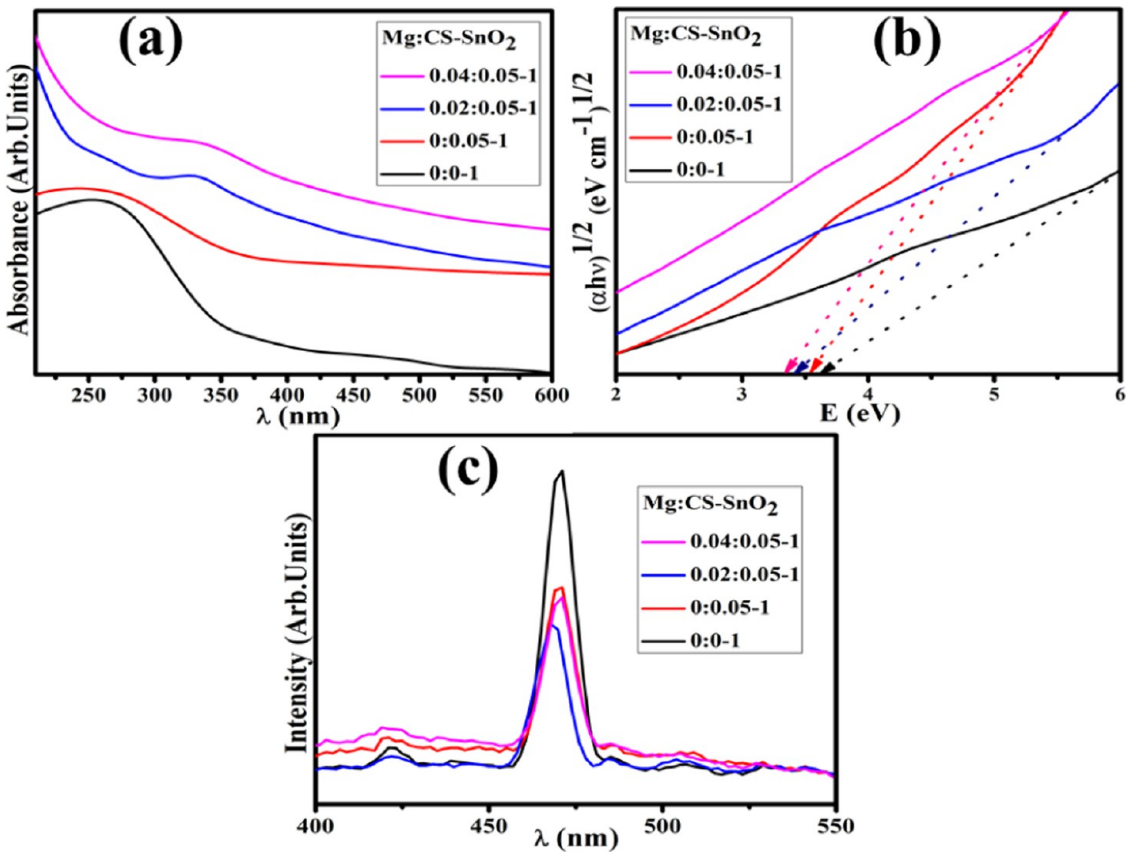

Figure 5. (a) UV−Vis spectra, (b) Tauc plot for band gap energy, (c) PL pattern of pristine and Mg/CS-doped SnO_2 QDs.

was increased by doping CS and Mg in SnO_2 because the crystallite size was reduced, as elaborated in Table 1.[31] The CA of SnO_2 was also increased as the crystallite size decreased, attributed to the large surface area of the catalyst.[31] Moreover, SAED analysis of primeval and doped samples revealed discrete and bright rings corresponding to different facets (110), (211), (101), and $(0\bar{2}1)$ of the XRD pattern, as elaborated in Figure 4c−f. These circular rings containing bright spots exhibited the polycrystalline nature of SnO_2, CS/SnO_2, and (2, 4 wt %) Mg/CS SnO_2. The crystallinity of the samples was reduced by the addition of CS and Mg, as divulged by the XRD data. The FTIR technique was used to investigate the functional groups in the pristine and Mg/CS-doped SnO_2 QDs, as demonstrated in Figure 4b. Pure SnO_2 QDs confirm the Sn−O−Sn bending and stretching and C−O stretching vibrations at 530, 640, and 2301 cm^{-1} bands, respectively.[32] The transmission bands at 3356 and 1633 cm^{-1} can be allocated to the O−H vibration.[33] Upon doping of CS, bands move toward the lower wavenumber, representing the presence of the −OH or NH_2 functional group in CS.[27] The transmittance band in the region of 3291−361 cm^{-1} corresponds to the N−H and O−H stretching that identifies the presence of CS.[34]

Figure 5a reveals the UV−Vis absorption spectra of pristine and Mg/CS-doped SnO_2 in the wavelength range from 250 to 600 nm. The acquired spectra delivered facts about Eg and optical characteristics of the synthesized semiconductors. For semiconductor nanostructures, particle size reduction causes the absorption band to move toward the larger energy, attributed to the quantum confinement effect. Consequently, the absorption band of SnO_2 observed at 263 nm corresponds to the n−σ^* electronic transition.[35,36] Tauc's relation has been used to calculate the Eg as 3.63, 3.56, 3.47, and 3.38 eV for SnO_2 and (2%, 4%) Mg/CS-doped QDs, as elaborated in Figure 5b.[33] Upon doping of Mg and CS, absorption enhanced toward a higher wavelength (red shift), representing a reduction in Eg because of a larger concentration of oxygen vacancies in SnO_2. Both the crystallite size and Eg decreased with CS and Mg doping due to the substitution of Mg^{2+} ions into SnO_2 QDs and matched well with those in the literature.[37−39] The reduction of Eg might be associated with the existence of holes in Mg-doped QDs. Due to the lower valence compared to that of Sn^{4+}, all substitutional Mg atoms will produce two holes in the O 2p state that may create an impurity band in the Eg region. First, electrons recombine with holes in the impurity band, and after that, confined electrons consecutively combined with holes in CB, which decreased the Eg.[40] Moreover, the PCA of semiconductors depends upon the reduction of Eg because a photon with sufficient energy is required to stimulate the electron from the VB to the CB. The e^-−h^+ pairs generated are utilized to lessen and oxidize chemicals, which results in enhancing the PCA.[41] As Eg of SnO_2 decreased by doping CS and Mg, its PCA was enhanced, as represented in Table 1. PL spectroscopy was used to elucidate the variation in the charge carrier efficiency of bare and Mg/CS-doped QDs, as depicted in Figure 5c. The photoluminescence is displayed when charge carrier recombination occurs at an excitation wavelength assigned to the coulombic interaction and increased emission.[32] The Stokes shift is the wavelength difference between the electronic and PL spectra that occurred due to the loss of vibrational energy in emission spectra. As a result, the wavelength of emission

https://doi.org/10.1021/acsomega.2c05133
ACS Omega 2022, 7, 46428−46439

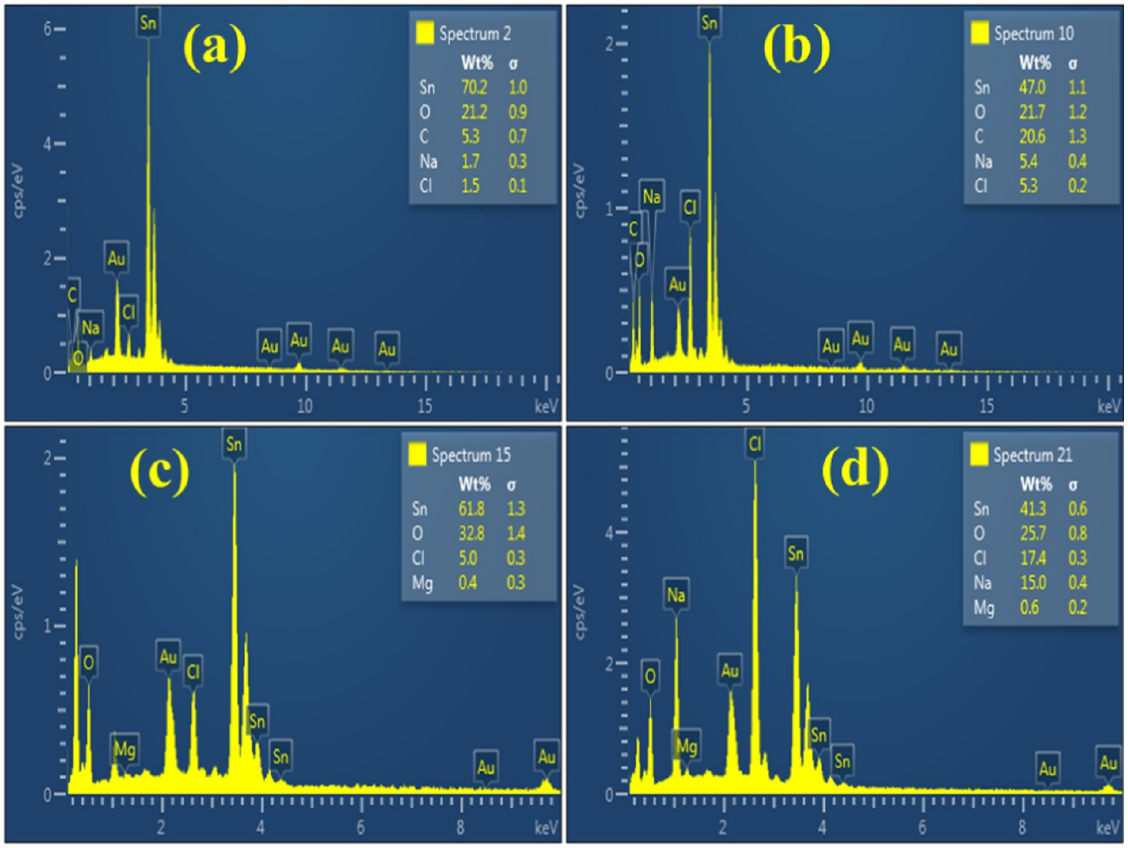

Figure 6. EDS analysis of (a) SnO_2, (b) CS-doped SnO_2, (c) 2% Mg/CS-doped SnO_2, (d) 4% Mg/CS-doped SnO_2 QDs.

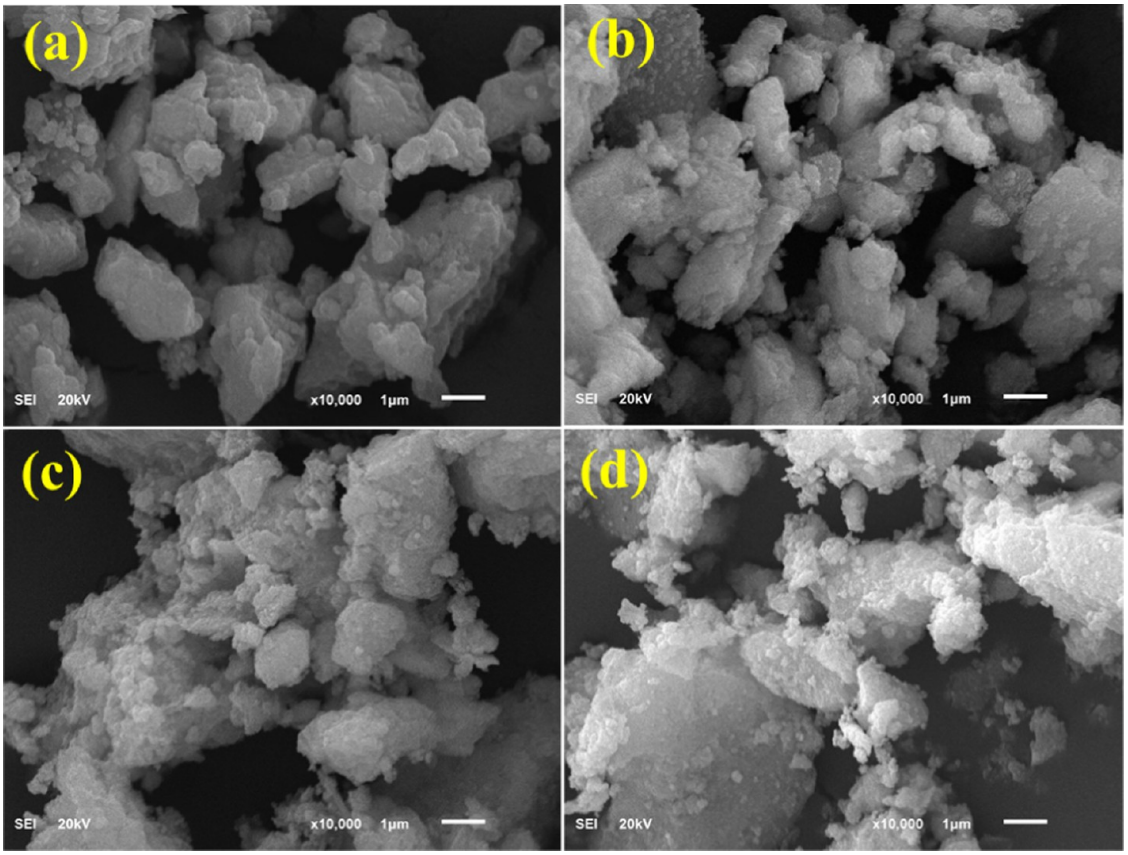

Figure 7. FESEM micrographs of (a) SnO_2, (b) CS-doped SnO_2, (c) 2% Mg/CS-doped SnO_2, and (d) 4% Mg/CS-doped SnO_2 QDs.

https://doi.org/10.1021/acsomega.2c05133
ACS Omega 2022, 7, 46428−46439

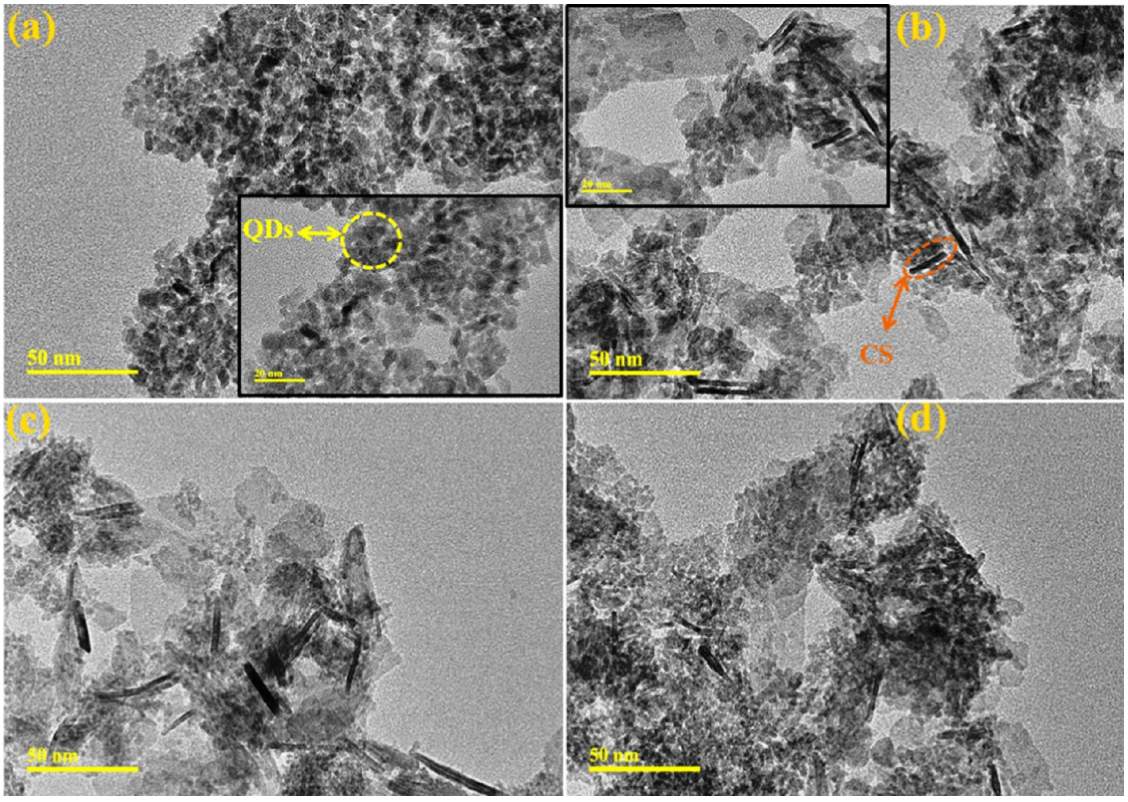

Figure 8. (a–d) TEM micrographs of (a) SnO_2, (b) CS-doped SnO_2, (c) 2% Mg/CS-doped SnO_2, and (d) 4% Mg/CS-doped SnO_2 QDs.

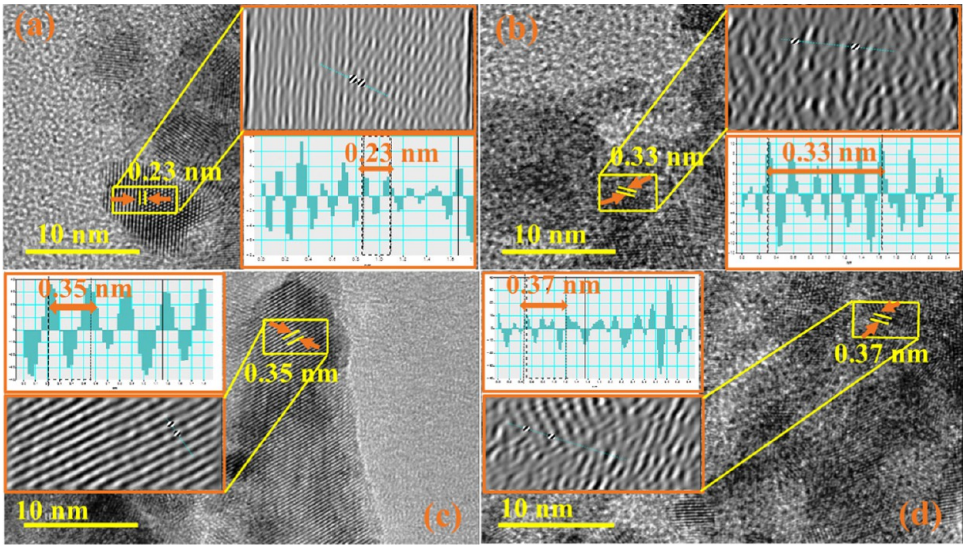

Figure 9. *d*-spacing from HR-TEM of (a) SnO_2, (b) CS-doped SnO_2, (c) 2% Mg/CS-doped SnO_2, and (d) 4% Mg/CS-doped SnO_2 QDs.

spectra increased and well matched with that in the literature.[42−44] SnO_2 shows a single high-intensity emission band in the visible region at 470 nm, which is attributed to the fluorescence phenomenon.[32] Upon addition of CS, the intensity was reduced, suggesting a low carrier recombination rate, and the peak intensity was further decreased by the incorporation of Mg, ascribed to the phosphorescence phenomena. Among all samples, 4% Mg/CS−SnO_2 has the lowest PL intensity, which signifies the largest charge carrier efficacy and remarkable PCA.[32]

EDS was analyzed to assess the chemical composition to confirm the purity of the synthesized photocatalysts. Figure 6a exhibits the EDS spectra of the pure sample and verifies the formation of Sn and O. Additional peaks of C and Mg, as depicted in Figure 6b−d, confirm the substitution of the dopant species. The Na peak is ascribed to utilizing NaOH to maintain the pH during the preparation of the samples. The Cl peak is assigned to the precursor for the synthesis of SnO_2. The formation of SnO_2 is further confirmed through FTIR analysis corresponding to the bending and stretching vibrations of Sn−O−Sn at 530 and 640 cm^{-1} bands, respectively, as represented in Figure 4b.

FESEM images of pure and CS/Mg-doped SnO_2 are given in Figure 7a−d. SnO_2 revealed nonuniform chunks with

https://doi.org/10.1021/acsomega.2c05133
ACS Omega 2022, 7, 46428−46439

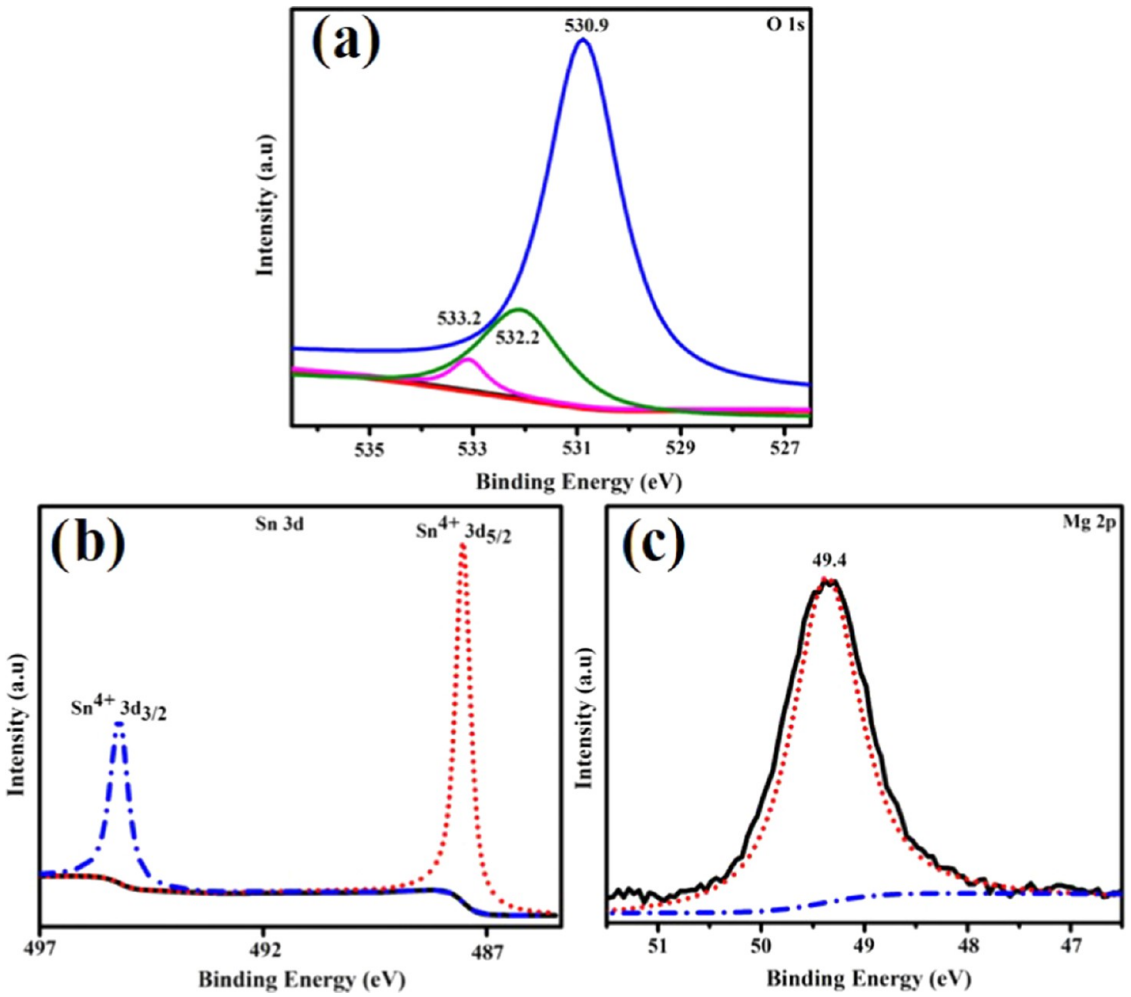

Figure 10. XPS spectra of Mg:CS−SnO_2, (a) O 1s of SnO_2, (b) Sn 3d, and (c) Mg 2p.

randomly distributed small-sized particles, as revealed in Figure 7a. Upon doping of CS, small-sized chunks with an increased quantity of nanosized particles were observed, as shown in Figure 7b. With the incorporation of Mg (2%), agglomerated small-sized particles were overlapped with chunks, and this pattern was increased with the higher concentration of Mg (4%) as elaborated in Figure 7c,d.

TEM analysis was undertaken to investigate the morphological features of the prepared photocatalysts. In Figure 8a, HR-TEM micrographs revealed the formation of the QDs of SnO_2. The addition of CS into QDs showed that few nanorod-like structures overlapped with QDs (Figure 8b), confirming the partial interaction between CS and QDs. Upon Mg (2%) doping (Figure 8c), agglomeration was observed, which increased with the higher concentration of Mg (4%) (Figure 8d). This led to Mg being appropriately dissolved in the binary system of CS and QDs, which is evident in the doped species. The average particle size of SnO_2 was decreased by incorporating CS and Mg, which enhanced the PCA of samples assigned to the large surface area of the small-sized photocatalyst, as represented in Table 1.

At a higher resolution (∼10 nm), HR-TEM microscopy was employed to calibrate the interlayer spacing of bare and doped SnO_2, as represented in Figure 9b−d. In Figure 9a, the measured *d*-spacing value of SnO_2 was ∼0.23 nm, which matches with the (200) facet and corresponds well with XRD. With the incorporation of CS and Mg, the interplanar spacing of QDs was slightly increased and found to be ∼0.33, 0.35, and 0.37 nm, in accordance with peak alteration with XRD as shown in Figure 9b−d.

The quantum dots were examined by X-ray photoelectron spectroscopy (XPS), as illustrated in Figure 10a−c, to identify their chemical structure and to validate Mg doping. The fitting findings of O1 enabled us to identify three components. The principal signal at 530.9 eV is close toward the binding energy of oxygen in SnO_2,[45,46] as presented in Figure 10a. Simultaneously, the remaining two low-intensity and high-energy components could be assigned to oxygen-containing adsorbates: OH groups (532.2 eV) and water molecules (533.2 eV) as shown in Figure 10a.[45−47] The existence of SnO_2 was established by the attribution of principal peaks at 487.4 and 495.8 eV corresponding to Sn $3d_{5/2}$ and Sn $3d_{3/2}$, separately, of Sn (IV), as illustrated in Figure 10b.[48] The high-resolution spectra reveal that the peak at 49.4 eV corresponds to the Mg^{2+} ion, showing excellent agreement with the findings provided for Mg $2p_{3/2}$ as depicted in Figure 10c.[48]

A comparative reduction efficiency of sonophotocatalysis, photocatalysis, and catalysis of MB solution was examined on pure and doped SnO_2 QDs, as demonstrated in Figure 11a−c. For SPCA, the largest competitive degradation of 99% occurs in basic medium (pH 12) within 120 min, whereas at the same time, degradation of 85.67 and 55.82% for the neutral (pH ∼

https://doi.org/10.1021/acsomega.2c05133
ACS Omega 2022, 7, 46428−46439

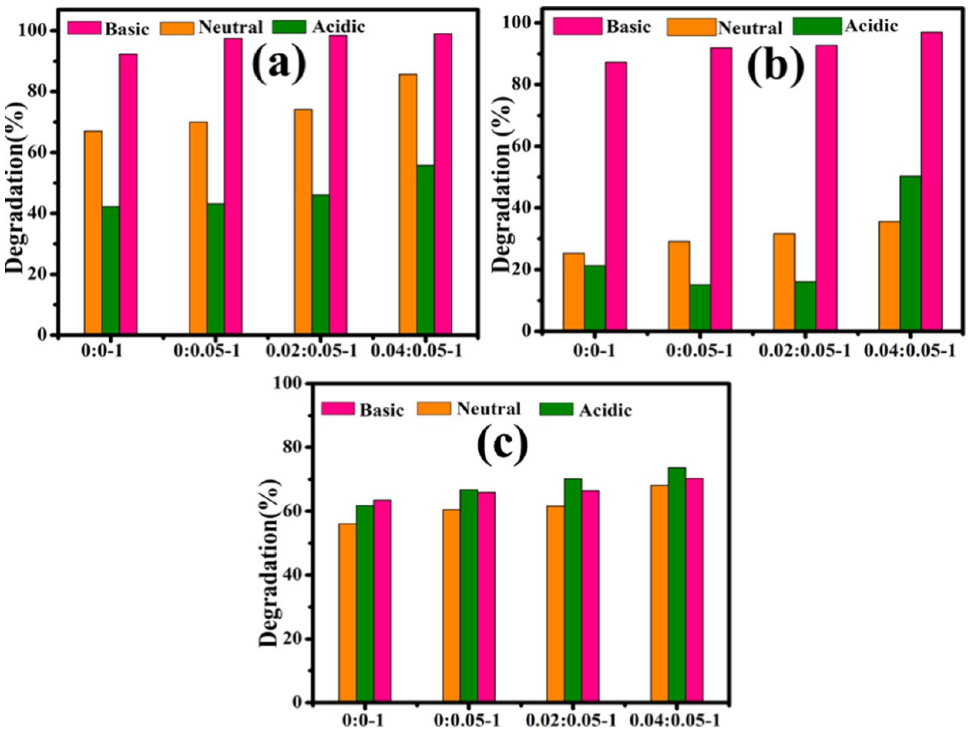

Figure 11. (a) Sonophotocatalysis, (b) photocatalysis, and (c) catalysis of Mg:CS−SnO_2 in acidic, basic, and neutral medium.

Table 2. Comparison of the Prepared Sonophotocatalysts with Other Reported Sonophotocatalysts

sonophotocatalyst	degradation efficiency (%)	reaction time	dyes	concentration of dye	refs
ZnO	54	100 min	methyl orange	50 mg/L	49
NiO	90	30 min	MB	200 mL of 20 mg/L	50
$MgTi_2O_5$	96	75 min	triphenylmethane dyes	100 mL of 5.32 mg/L	51
polyacrylonitrile/g-C_3N_4/CdS heterojunction	92	15 min	rhodamine B	100 mL of 10 mg/L	52
Bi_2O_3	67	60 min	basic brown 1	500 mL of 10 mg/L	53
graphene nanoribbon-CeO_2 heterojunction	91.2	120 min	tetracycline hydrochloride	20 mg/L	54
$CeO_2/TiO_2/SiO_2$	90.8	1.3 h	chlorpyrifos	1−6 mg/L	55
Co doped Fe_2O_3	82	90 min	eosin B	250 mL of 5.32 mg/L	56
Mg:CS−SnO_2	99	120 min	MB	1 g/ mL	present study

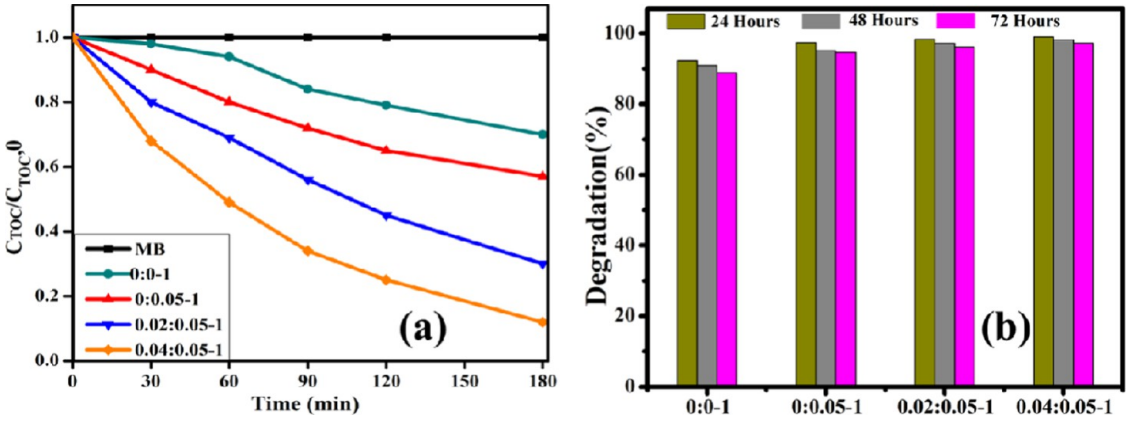

Figure 12. (a) Mineralization (TOC) of MB solution. (b) Stability of pristine and Mg/CS-doped SnO_2 in basic medium.

7) and acidic medium (pH ∼ 4) was noted, respectively, as displayed in Figure 11a. For PCA, the optimum reduction of dye was 96% in the basic medium, whereas 35.6 and 50.35% for the neutral and acidic medium were noted, respectively, as elaborated in Figure 11b. Figure 11c demonstrates that the CA of pristine and CS/Mg-doped SnO_2 QDs revealed the optimum reduction of 61.81−73.64% in acidic medium, 63.49−70.26% in basic medium, and 56.11−68.14% in neutral medium. The pH of the solution controlled the PCA. Owing to the cationic nature of MB, its degradation was smaller at low

https://doi.org/10.1021/acsomega.2c05133
ACS Omega 2022, 7, 46428−46439

pH and maximum at higher pH. In an acidic dye solution, adsorption of cationic species is limited and attributed to a positively charged catalyst surface. The adsorption of MB dye enhanced in basic medium, manifesting the large electrostatic interaction between the MB dye and negatively charged catalyst that causes the surface charges to become negative.[39] Moreover, the addition of CS enhanced the photocatalytic degradation of MB, attributed to the occurrence of amino and hydroxyl groups in CS.[38] The incorporation of Mg also enhanced the PCA, which served as an electron acceptor and separated the e^-−h^+ pair; consequently, the trapped electron shifted to absorb the oxygen molecule. Simultaneously, more dye molecules are absorbed on the surfaces of Mg/CS-doped SnO_2 that enhance dye reduction.[37] Moreover, the CA of SnO_2 is enhanced by adding CS, which is attributed to possessing a large number of active sites.[36] The result indicated that 4% Mg/CS-doped SnO_2 shows optimum (99%) sonophotocatalytic degradation of MB in basic medium compared to photocatalytic and catalytic degradation. From these outcomes, we deduce that SnO_2 QDs proved to be an excellent material for the degradation of the MB dye by the sonophotocatalysis process. Table 2 presents the comparison of the prepared sonophotocatalyst with other reported sonophotocatalysts in terms of percentage degradation, reaction time, and concentration of dyes.

A total organic carbon (TOC) assessment of treated water was conducted for the estimation of the dye (MB) degree of mineralization. The study was performed on Mg/CS-doped SnO_2 using varying time intervals up to 180 min. This analysis (Figure 12a) demonstrated that TOC of the MB solution treated with the synthesized compounds under visible light irradiation reduced continuously with reaction time, and a significant amount of mineralization of the dye was found after 180 min in Mg:CS−SnO_2 (0.04:0.05-1). To check the stability of the photocatalyst, the degraded solution was kept in the absence of light for three days to see whether the dye decolorization was stable or not in the presence of a catalyst. An UV−Vis spectrophotometer was utilized to monitor the dye reduction efficiency every 24 h, as shown in Figure 12b. The % reduction efficiency was calculated using eq 1.

The prepared samples are stable up to three cycles as shown in Figure 12. Additionally, the stability of 4% Mg/CS-doped SnO_2 was also examined through XRD before and after the sonophotocatalytic reaction as depicted in Figure 13. The crystallinity of QDs was decreased after the 3rd cycle because of photodissolution and photocorrosion of the photocatalyst.[57]

DPPH scavenging was used to examine and quantify the antioxidant effects of active radical species (Figure 14.). Antioxidant properties of compounds are interrelated with their potential to transfer hydrogen or electrons atoms to the DPPH free radical, resulting in stable diamagnetic compounds. The ability of free radical reduction of this DPPH can be evaluated spectrophotometrically by measuring the degradation in absorbance (517 nm). The antioxidant activity of all prepared samples exhibited a dose-dependent behavior. Mg:CS−SnO_2 (0.04:0.05-1) displayed the highest scavenging performance up to 71.45% at 500 μg/mL concentration and scavenged DPPH radicals through the donation of hydrogen atoms. The formed highly reactive $^{\bullet}OH$ and $^{\bullet}O_2$ radical species can interact with DPPH free radicals and result in its degradation, which is highly correlated with the standard (ascorbic acid).[58]

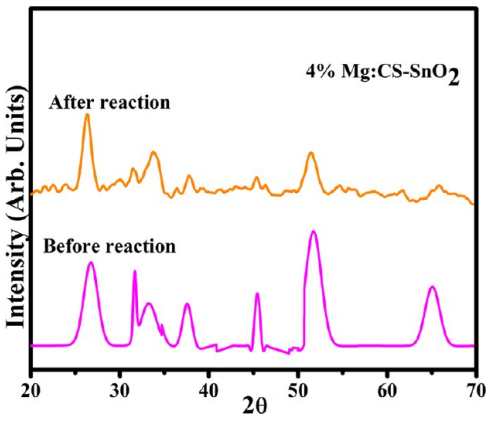

Figure 13. XRD of 4%Mg:CS−SnO2 before and after SPCA.

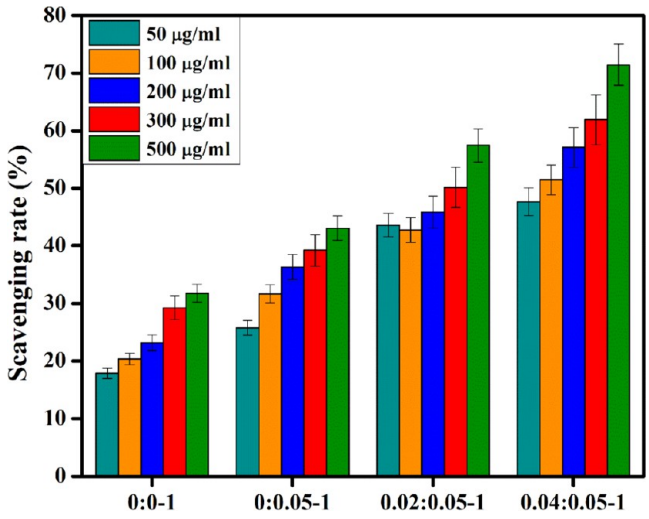

Figure 14. Mg:CS−SnO_2 DPPH scavenging activity.

4. CONCLUSIONS

In this study, SnO_2 and Mg/CS-doped SnO_2 were effectively synthesized by a hydrothermal method to compare the MB reduction efficiency by sonophotocatalytic, photocatalytic, and catalytic processes. Among the samples, 4% Mg/CS-doped SnO_2 QDs show a maximum of 99% sonophotocatalytic degradation of MB in basic medium compared to other activities. The XRD pattern verified the tetragonal configurations of SnO_2, and crystallite size decreased from 9.02 to 5.56 nm upon the incorporation of CS and Mg. Meanwhile, FTIR and SAED analysis endorsed Sn−O−Sn vibration at 530 and 640 cm^{-1} and crystalline behavior. The TEM image elucidates the formation of QDs of SnO_2, and upon doping of CS, a rod-like structure formed, which partially interacts with QDs. The calculated *d*-spacing was ∼0.23, 0.33, 0.35, and 0.37 nm for both pristine and Mg/CS-doped SnO_2. The Eg of SnO_2 was observed to be 3.63 eV, and upon doping of Mg and CS, Eg reduced to 3.38 eV. In conclusion, Mg/CS-doped SnO_2 QDs were found to be an effective material for the sonophotocatalytic degradation of the MB dye.

AUTHOR INFORMATION

Corresponding Authors

Muhammad Ikram − *Solar Cell Applications Research Lab, Department of Physics, Government College University Lahore, Lahore 54000 Punjab, Pakistan;* orcid.org/0000-

https://doi.org/10.1021/acsomega.2c05133
ACS Omega 2022, 7, 46428−46439

0001-7741-789X; Email: dr.muhammadikram@gcu.edu.pk

Walid Nabgan − *Departament d'Enginyeria Química, Universitat Rovira i Virgili, 43007 Tarragona, Spain*; Email: walid.nabgan@urv.cat

Authors

Sawaira Moeen − *Solar Cell Applications Research Lab, Department of Physics, Government College University Lahore, Lahore 54000 Punjab, Pakistan*

Ali Haider − *Department of Clinical Sciences, Faculty of Veterinary and Animal Sciences, Muhammad Nawaz Shareef University of Agriculture (MNSUA), Multan 66000, Pakistan*

Junaid Haider − *Tianjin Institute of Industrial Biotechnology, Chinese Academy of Sciences, Tianjin 300308, China*; orcid.org/0000-0002-2254-1196

Anwar Ul-Hamid − *Center for Engineering Research, Research Institute, King Fahd University of Petroleum & Minerals, Dhahran 31261, Saudi Arabia*; orcid.org/0000-0002-0259-301X

Tahira Shujah − *Department of Physics, University of Central Punjab, Lahore 54000, Pakistan*

Misbah Naz − *Department of Chemistry, University of Education, Lahore 54000, Pakistan*

Iram Shahzadi − *Punjab University College of Pharmacy, University of the Punjab, 54000 Lahore, Pakistan*

Complete contact information is available at: https://pubs.acs.org/10.1021/acsomega.2c05133

Notes

The authors declare no competing financial interest.

■ ACKNOWLEDGMENTS

The authors are thankful to higher education commission (HEC), Pakistan, via the National Research Program for Universities (NRPU) Project-20-17615 (Dr. Muhammad Ikram).

■ REFERENCES

(1) Raza, A.; Ikram, M.; Aqeel, M.; Imran, M.; Ul-Hamid, A.; Riaz, K. N.; Ali, S. Enhanced Industrial Dye Degradation Using Co Doped in Chemically Exfoliated MoS2 Nanosheets. *Appl. Nanosci.* **2020**, *10*, 1535−1544.

(2) Han, S.; Liu, K.; Hu, L.; Teng, F.; Yu, P.; Zhu, Y. Corrigendum: Superior Adsorption and Regenerable Dye Adsorbent Based on Flower-Like Molybdenum Disulfide Nanostructure. *Sci. Rep.* **2017**, *7*, No. 46887.

(3) Sharma, M.; Behl, K.; Nigam, S.; Joshi, M. TiO2-GO Nanocomposite for Photocatalysis and Environmental Applications: A Green Synthesis Approach. *Vacuum* **2018**, *156*, 434−439.

(4) Oppong, S. O. B.; Opoku, F.; Anku, W. W.; Kiarii, E. M.; Govender, P. P. Experimental and Computational Design of Highly Active Ce−ZrO 2 −GO Photocatalyst for Eosin Yellow Dye Degradation: The Role of Interface and Ce 3+ Ion. *Catal. Lett.* **2019**, *149*, 1633−1650.

(5) Kunduru, K. R.; Nazarkovsky, M.; Farah, S.; Pawar, R. P.; Basu, A.; Domb, A. J. Nanotechnology for Water Purification: Applications of Nanotechnology Methods in Wastewater Treatment. *Water Purif.* **2017**, 33−74.

(6) Junaid, M.; Imran, M.; Ikram, M.; Naz, M.; Aqeel, M.; Afzal, H.; Majeed, H.; Ali, S. The Study of Fe-Doped CdS Nanoparticle-Assisted Photocatalytic Degradation of Organic Dye in Wastewater. *Appl. Nanosci.* **2019**, *9*, 1593−1602.

(7) Kim, S. P.; Choi, M. Y.; Choi, H. C. Photocatalytic Activity of SnO2 Nanoparticles in Methylene Blue Degradation. *Mater. Res. Bull.* **2016**, *74*, 85−89.

(8) Hassani, A.; Krishnan, S.; Scaria, J.; Eghbali, P.; Nidheesh, P. V. Z-Scheme Photocatalysts for Visible-Light-Driven Pollutants Degradation: A Review on Recent Advancements. *Curr. Opin. Solid State Mater. Sci.* **2021**, *25*, 100941.

(9) Modirshahla, N.; Behnajady, M. A.; Rahbarfam, R.; Hassani, A. Effects of Operational Parameters on Decolorization of C. I. Acid Red 88 by UV/H 2O 2 Process: Evaluation of Electrical Energy Consumption. *Clean - Soil, Air, Water* **2012**, *40*, 298−302.

(10) Hassani, A.; Faraji, M.; Eghbali, P. Facile Fabrication of Mpg-C3N4/Ag/ZnO Nanowires/Zn Photocatalyst Plates for Photodegradation of Dye Pollutant. *J. Photochem. Photobiol. A Chem.* **2020**, 400.

(11) Serhan, M.; Sprowls, M.; Jackemeyer, D.; Long, M.; Perez, I. D.; Maret, W.; Tao, N.; Forzani, E., *Total Iron Measurement in Human Serum with a Smartphone*, AIChE Annual Meeting, Conference Proceedings, 2019; pp 1−3.

(12) Ikram, M.; Hassan, J.; Raza, A.; Haider, A.; Naz, S.; Ul-Hamid, A.; Haider, J.; Shahzadi, I.; Qamar, U.; Ali, S. Photocatalytic and Bactericidal Properties and Molecular Docking Analysis of TiO2nanoparticles Conjugated with Zr for Environmental Remediation. *RSC Adv.* **2020**, *10*, 30007−30024.

(13) Ikram, M.; Hayat, S.; Imran, M.; Haider, A.; Naz, S.; Ul-Hamid, A.; Shahzadi, I.; Haider, J.; Shahzadi, A.; Nabgan, W.; Ali, S. Novel Ag/Cellulose-Doped CeO2 Quantum Dots for Efficient Dye Degradation and Bactericidal Activity with Molecular Docking Study. *Carbohydr. Polym.* **2021**, *269*, 118346.

(14) Aqeel, M.; Rashid, M.; Ikram, M.; Haider, A.; Naz, S.; Haider, J.; Ul-Hamid, A.; Shahzadi, A. Photocatalytic, Dye Degradation, and Bactericidal Behavior of Cu-Doped ZnO Nanorods and Their Molecular Docking Analysis. *Dalton Trans.* **2020**, *49*, 8314−8330.

(15) Van Viet, P.; Thi, C. M.; Van Hieu, L. The High Photocatalytic Activity of SnO2 Nanoparticles Synthesized by Hydrothermal Method. *J. Nanomater* **2016**, *2016*, 1−8.

(16) Kale, V.; Hunge, Y. M.; Kamble, S. A.; Deshmukh, M.; Bhoraskar, S. V.; Mathe, V. L. Modification of Energy Level Diagram of Nano-Crystalline ZnO by Its Composites with ZnWO4 Suitable for Sunlight Assisted Photo Catalytic Activity. *Mater. Today Commun.* **2021**, *26*, 102101.

(17) Ikram, M.; Aslam, S.; Haider, A.; Naz, S.; Ul-Hamid, A.; Shahzadi, A.; Ikram, M.; Haider, J.; Ahmad, S. O. A.; Butt, A. R. Doping of Mg on ZnO Nanorods Demonstrated Improved Photocatalytic Degradation and Antimicrobial Potential with Molecular Docking Analysis. *Nanoscale Res. Lett.* **2021**, *16*, 78.

(18) Asaithambi, S.; Sakthivel, P.; Karuppaiah, M.; Hayakawa, Y.; Loganathan, A.; Ravi, G. Improved Photocatalytic Performance of Nanostructured SnO2 via Addition of Alkaline Earth Metals (Ba2+, Ca2+ and Mg2+) under Visible Light Irradiation. *Appl. Phys. A* **2020**, *126*, 265.

(19) Sokker, H. H.; El-Sawy, N. M.; Hassan, M. A.; El-Anadouli, B. E. Adsorption of Crude Oil from Aqueous Solution by Hydrogel of Chitosan Based Polyacrylamide Prepared by Radiation Induced Graft Polymerization. *J. Hazard. Mater.* **2011**, *190*, 359−365.

(20) Nawi, M. A.; Sabar, S.; Jawad, A. H.; Sheilatina; Ngah, W. S. W. Adsorption of Reactive Red 4 by Immobilized Chitosan on Glass Plates: Towards the Design of Immobilized TiO2-Chitosan Synergistic Photocatalyst-Adsorption Bilayer System. *Biochem. Eng. J.* **2010**, *49*, 317−325.

(21) Guo, Q.; Zhou, C.; Ma, Z.; Yang, X. Fundamentals of TiO2 Photocatalysis: Concepts, Mechanisms, and Challenges. *Adv. Mater.* **2019**, *31*, 1901997.

(22) Laoufi, N. A.; Tassalit, D.; Bentahar, F. The Degradation of Phenol in Water Solution by TiO2 Photocatalysis in a Helical Reactor. *Glob. Nest J.* **2008**, *10*, 404−418.

(23) Moma, J.; Baloyi, J.Modified Titanium Dioxide for Photocatalytic Applications. In *Photocatalysts - Applications and Attributes*, 2019.

(24) Karuppaiah, M.; Sakthivel, P.; Asaithambi, S.; Murugan, R.; Yuvakkumar, R.; Ravi, G. Formation of One Dimensional Nanorods with Microsphere of MnCO 3 Using Ag as Dopant to Enhance the Performance of Pseudocapacitors. *Mater. Chem. Phys.* **2019**, *228*, 1−8.
(25) Ikram, M.; Umar, E.; Raza, A.; Haider, A.; Naz, S.; Ul-Hamid, A.; Haider, J.; Shahzadi, I.; Hassan, J.; Ali, S. Dye Degradation Performance, Bactericidal Behavior and Molecular Docking Analysis of Cu-Doped TiO2nanoparticles. *RSC Adv.* **2020**, *10*, 24215−24233.
(26) Bezzerrouk, M. A.; Bousmaha, M.; Hassan, M.; Akriche, A.; Kharroubi, B.; Naceur, R.; Guezzoul, M. Enhanced Methylene Blue Removal Efficiency of SnO2 Thin Film Using Sono-Photocatalytic Processes. *Opt. Mater.* **2021**, *117*, No. 111116.
(27) Gupta, V. K.; Saravanan, R.; Agarwal, S.; Gracia, F.; Khan, M. M.; Qin, J.; Mangalaraja, R. V. Degradation of Azo Dyes under Different Wavelengths of UV Light with Chitosan-SnO2 Nanocomposites. *J. Mol. Liq.* **2017**, *232*, 423−430.
(28) Weng, Y.; Deng, D.; Zhang, L.; Su, Y.; Lv, Y. A Cataluminescence Gas Sensor Based on Mesoporous Mg-Doped SnO2 Structures for Detection of Gaseous Acetone. *Anal. Methods* **2016**, *8*, 7816−7823.
(29) Pavitra, V.; Udayabhanu; Harini, R.; Viswanatha, R.; Praveen, B. M.; Nagaraju, G. Sonochemical Synthesis of SnO2−CuO Nanocomposite: Diverse Applications on Li-Ion Battery, Electrochemical Sensing and Photocatalytic Activity. *J. Mater. Sci. Mater. Electron.* **2020**, *31*, 8737−8749.
(30) Gupta, V. K.; Saravanan, R.; Agarwal, S.; Gracia, F.; Khan, M. M.; Qin, J.; Mangalaraja, R. V. Degradation of Azo Dyes under Different Wavelengths of UV Light with Chitosan-SnO2 Nanocomposites. *J. Mol. Liq.* **2017**, *232*, 423−430.
(31) Luque, P. A.; Nava, O.; Soto-Robles, C. A.; Garrafa-Galvez, H. E.; Martínez-Rosas, M. E.; Chinchillas-Chinchillas, M. J.; Vilchis-Nestor, A. R.; Castro-Beltrán, A. SnO2 Nanoparticles Synthesized with Citrus Aurantifolia and Their Performance in Photocatalysis. *J. Mater. Sci. Mater. Electron.* **2020**, *31*, 16859−16866.
(32) Zulfiqar; Yuan, Y.; Jiang, Q.; Yang, J.; Feng, L.; Wang, W.; Ye, Z.; Lu, J. Variation in Luminescence and Bandgap of Zn-Doped SnO2 Nanoparticles with Thermal Decomposition. *J. Mater. Sci. Mater. Electron.* **2016**, *27*, 9541−9549.
(33) Haridas, D.; Chowdhuri, A.; Sreenivas, K.; Gupta, V. Effect of Thickness of Platinum Catalyst Clusters on Response of SnO 2 Thin Film Sensor for LPG. Sensors Actuators. *Sens. Actuators, B* **2011**, *153*, 89−95.
(34) Queiroz, M. F.; Melo, K. R. T.; Sabry, D. A.; Sassaki, G. L.; Rocha, H. A. O. Does the Use of Chitosan Contribute to Oxalate Kidney Stone Formation? *Mar. Drugs* **2015**, *13*, 141−158.
(35) Selvi, N.; Sankar, S.; Dinakaran, K. Interfacial Effect on the Structural and Optical Properties of Pure SnO2 and Dual Shells (ZnO; SiO2) Coated SnO2 Core-Shell Nanospheres for Optoelectronic Applications. *Superlattices Microstruct.* **2014**, *76*, 277−287.
(36) Bari, A.; Ikram, M.; Haider, A.; Ul-Hamid, A.; Haider, J.; Shahzadi, I.; Nazir, G.; Shahzadi, A.; Imran, M.; Ghaffar, A. Evaluation of Bactericidal Potential and Catalytic Dye Degradation of Multiple Morphology Based Chitosan/Polyvinylpyrrolidone-Doped Bismuth Oxide Nanostructures. *Nanoscale Adv.* **2022**, *4*, 2713−2728.
(37) Vadivel, S.; Rajarajan, G. Effect of Mg Doping on Structural, Optical and Photocatalytic Activity of SnO2 Nanostructure Thin Films. *J. Mater. Sci. Mater. Electron.* **2015**, *26*, 3155−3162.
(38) Gupta, V. K.; Saravanan, R.; Agarwal, S.; Gracia, F.; Khan, M. M.; Qin, J.; Mangalaraja, R. V. Degradation of Azo Dyes under Different Wavelengths of UV Light with Chitosan-SnO2 Nanocomposites. *J. Mol. Liq.* **2017**, *232*, 423−430.
(39) Jamal, F.; Ikram, M.; Haider, A.; Ul-Hamid, A.; Ijaz, M.; Nabgan, W.; Haider, J.; Shahzadi, I. Facile Synthesis of Silver and Polyacrylic Acid Doped Magnesium Oxide Nanostructure for Photocatalytic Dye Degradation and Bactericidal Behavior. *Appl. Nanosci.* **2022**, DOI: 10.1007/s13204-022-02504-8.
(40) Vadivel, S.; Rajarajan, G. Effect of Mg Doping on Structural, Optical and Photocatalytic Activity of SnO2 Nanostructure Thin Films. *J. Mater. Sci. Mater. Electron.* **2015**, *26*, 3155−3162.
(41) Parthibavarman, M.; Sathishkumar, S.; Jayashree, M.; BoopathiRaja, R. Microwave Assisted Synthesis of Pure and Ag Doped SnO 2 Quantum Dots as Novel Platform for High Photocatalytic Activity Performance. *J. Clust. Sci.* **2019**, *30*, 351−363.
(42) Jayapandi, S.; Packiyaraj, P.; Premkumar, S.; Mayandi, J.; Anitha, K. Influence of PH in La-Doped SnO2 Nanoparticles towards Sensor Applications. *Ionics* **2017**, *23*, 2909−2917.
(43) Santana, N. D. C.; López, A.; Sosman, L. P.; Pedro, S. S. Broadband Photoluminescence in a Ceramic (Mg2SnO4−SnO2):Cr3+ System. *SN Appl. Sci.* **2021**, *3*, 125.
(44) Karpagam, S.; Guhanathan, S. Emitting Oligomer Containing Quinoline Group: Synthesis and Photophysical Properties of Conjugated Oligomer Obtained by Wittig Reaction. *J. Lumin.* **2014**, *145*, 752−759.
(45) Chuvenkova, O. A.; Domashevskaya, E. P.; Ryabtsev, S. V.; Yurakov, Y. A.; Popov, A. E.; Koyuda, D. A.; Nesterov, D. N.; Spirin, D. E.; Ovsyannikov, R. Y.; Turishchev, S. Y. XANES and XPS Investigations of Surface Defects in Wire-like SnO2 Crystals. *Phys. Solid State* **2015**, *57*, 153−161.
(46) Kuddus, M. A.; Rahman, A. Analysis of COVID-19 Using a Modified SLIR Model with Nonlinear Incidence. *Results Phys.* **2021**, *27*, 104478.
(47) Jerdev, D. I.; Koel, B. E. Oxidation of Ordered Pt-Sn Surface Alloys by O2. *Surf. Sci.* **2001**, *492*, 106−114.
(48) Xu, J. M.; Li, L.; Wang, S.; Ding, H. L.; Zhang, Y. X.; Li, G. H. Influence of Sb Doping on the Structural and Optical Properties of Tin Oxide Nanocrystals. *CrystEngComm* **2013**, *15*, 3296−3300.
(49) Yang, R.; Wu, Z.; Yang, Y.; Li, Y.; Zhang, L.; Yu, B. Understanding the Origin of Synergistic Catalytic Activities for ZnO Based Sonophotocatalytic Degradation of Methyl Orange. *J. Taiwan Inst. Chem. Eng.* **2021**, *119*, 128−135.
(50) Darbandi, M.; Eynollahi, M.; Badri, N.; Mohajer, M. F.; Li, Z. A. NiO Nanoparticles with Superior Sonophotocatalytic Performance in Organic Pollutant Degradation. *J. Alloys Compd.* **2022**, *889*, 161706.
(51) Selvamani, T.; Anandan, S.; et al. Preparation of MgTi2O5 Nanoparticles for Sonophotocatalytic Degradation of Triphenylmethane Dyes. *Ultrason. Sonochem.* **2021**, *75*, 105585.
(52) Zhang, J.; Zhao, W.; Pan, J.; Tang, R. The Sono-Photocatalytic Performance of PAN/g-C3N4/CdS Nanofibers Heterojunction. *Materials* **2021**, *14*, 5959.
(53) Dinesh, G. K.; Anandan, S.; Sivasankar, T. Synthesis of Fe-Doped Bi2O3 Nanocatalyst and Its Sonophotocatalytic Activity on Synthetic Dye and Real Textile Wastewater. *Environ. Sci. Pollut. Res.* **2016**, *23*, 20100−20110.
(54) Swamy, N. K.; Mohana, K. N. S.; Yashas, S. R.GNR@CeO2 Heterojunction as a Novel Sonophotocatalyst: Degradation of Tetracycline Hydrochloride, Kinetic Modeling and Synergistic Effects. *Colloids Surf., A***2022**, *639*. DOI: 10.1016/j.colsurfa.2022.128324.
(55) Mansourian, R.; Mousavi, S. M.; Alizadeh, S.; Sabbaghi, S. CeO2/TiO2/SiO2 Nanocatalyst for the Photocatalytic and Sonophotocatalytic Degradation of Chlorpyrifos. Can. *J. Chem. Eng.* **2022**, *100*, 451−464.
(56) Sharfalddin, A.; Alzahrani, E.; Alamoudi, M. Micro, Sono, Photocatalytic Degradation of Eosin B Using Ferric Oxide Doped with Cobalt. *Am. Chem. Sci. J.* **2016**, *13*, 1−13.
(57) Prakash, K.; Senthil Kumar, P.; Pandiaraj, S.; Saravanakumar, K.; Karuthapandian, S. Controllable Synthesis of SnO2 Photocatalyst with Superior Photocatalytic Activity for the Degradation of Methylene Blue Dye Solution. *J. Exp. Nanosci.* **2016**, *11*, 1138−1155.
(58) Kandiah, K.; Jeevanantham, T.; Ramasamy, B. Reliability of Antioxidant Potential and in Vivo Compatibility with Extremophilic Actinobacterial-Mediated Magnesium Oxide Nanoparticle Synthesis. *Artif. Cells, Nanomed., Biotechnol.* **2019**, *47*, 862−872.

https://doi.org/10.1021/acsomega.2c05133
ACS Omega 2022, 7, 46428−46439